



This is a repository copy of *Competition between two high- and low-affinity protein-binding sites in myosin VI controls its cellular function..*

White Rose Research Online URL for this paper:
<https://eprints.whiterose.ac.uk/153949/>

Version: Published Version

Article:

Fili, N., Hari-Gupta, Y., Aston, B. et al. (6 more authors) (2020) Competition between two high- and low-affinity protein-binding sites in myosin VI controls its cellular function. *Journal of Biological Chemistry*, 295 (2). pp. 337-347. ISSN 0021-9258

<https://doi.org/10.1074/jbc.ra119.010142>

Reuse

This article is distributed under the terms of the Creative Commons Attribution (CC BY) licence. This licence allows you to distribute, remix, tweak, and build upon the work, even commercially, as long as you credit the authors for the original work. More information and the full terms of the licence here:
<https://creativecommons.org/licenses/>

Takedown

If you consider content in White Rose Research Online to be in breach of UK law, please notify us by emailing eprints@whiterose.ac.uk including the URL of the record and the reason for the withdrawal request.



eprints@whiterose.ac.uk
<https://eprints.whiterose.ac.uk/>

Competition between two high- and low-affinity protein-binding sites in myosin VI controls its cellular function

Received for publication, July 10, 2019, and in revised form, November 15, 2019. Published, Papers in Press, November 19, 2019, DOI 10.1074/jbc.RA119.010142

Natalia Fili^{†1}, Yukti Hari-Gupta^{S1}, Bjork Aston^S,  Ália dos Santos[‡],  Rosemarie E. Gough[‡], Bana Alamad^S,  Lin Wang[¶], Marisa L. Martin-Fernandez[¶], and Christopher P. Toseland^{‡2}

From the [‡]Sheffield Cancer Centre, Department of Oncology and Metabolism, University of Sheffield, Sheffield S10 2RX, United Kingdom, the ^SSchool of Biosciences, University of Kent, Canterbury CT2 7NZ, United Kingdom, and the [¶]Central Laser Facility, Research Complex at Harwell, Science and Technology Facilities Council, Rutherford Appleton Laboratory, Harwell, Didcot, Oxford OX11 0QX, United Kingdom

Edited by Enrique M. De La Cruz

Myosin VI is involved in many cellular processes ranging from endocytosis to transcription. This multifunctional potential is achieved through alternative isoform splicing and through interactions of myosin VI with a diverse network of binding partners. However, the interplay between these two modes of regulation remains unexplored. To this end, we compared two different binding partners and their interactions with myosin VI by exploring the kinetic properties of recombinant proteins and their distribution in mammalian cells using fluorescence imaging. We found that selectivity for these binding partners is achieved through a high-affinity motif and a low-affinity motif within myosin VI. These two motifs allow competition among partners for myosin VI. Exploring how this competition affects the activity of nuclear myosin VI, we demonstrate the impact of a concentration-driven interaction with the low-affinity binding partner DAB2, finding that this interaction blocks the ability of nuclear myosin VI to bind DNA and its transcriptional activity *in vitro*. We conclude that loss of DAB2, a tumor suppressor, may enhance myosin VI-mediated transcription. We propose that the frequent loss of specific myosin VI partner proteins during the onset of cancer leads to a higher level of nuclear myosin VI activity.

Myosin VI (MVI)³ is an actin-based molecular motor that performs numerous vital roles in key cellular processes such as cell migration, endocytosis, exocytosis, and transcription (1–3). Defects in MVI lead to various diseases including hypertrophic cardiomyopathy, deafness, and cancer (4–7).

MVI consists of the highly conserved actin-binding motor domain, a neck region, and a C-terminal globular cargo-binding domain (CBD) (see Fig. 1a). We have recently shown that

MVI can adopt a back-folded conformation, in which the CBD is brought in close proximity to the motor domain (see Fig. 1b) (3). Moreover, two regions within the tail (MVI_{TAIL}, aa 814–1253) can be alternatively spliced, resulting in a 31-residue insertion (large insert, LI) adjacent to the CBD and/or an 9-residue insertion in the middle of the CBD (small insert, SI) (8). This leads to several splice isoforms, namely the noninsert (NI), SI, LI, and LI + SI, each with distinct intracellular distributions and functions (8, 9). For example, the NI isoform is able to enter the nucleus, whereas the LI is confined to the cell periphery (3).

The intracellular localization and function of MVI is also regulated through its interaction with a broad range of binding partners, such as DAB2 (disabled-2), GIPC (GAIP-interacting protein C terminus), and NDP52 (nuclear dot protein 52). These partners specifically bind to one of two established motifs within the CBD of MVI, namely the RRL and WWY (10–12).

NDP52, also known as CALCOCO2, is an RRL-binding partner of MVI. It was initially identified in the nucleus (13), but it was later found to be mostly cytoplasmic (14), with roles in cell adhesion and autophagy (10, 15). NDP52 has been shown to release the back-folded conformation of MVI, allowing MVI to dimerize and to interact with DNA, both of which enable coupling of MVI to RNA polymerase II. Moreover, NDP52 has been shown to have a role in regulating transcription (3), possibly as a coactivator, similarly to its highly conserved family member CoCoA (16).

DAB2, also known as DOC-2 (differentially expressed in ovarian carcinoma), links MVI to clathrin-coated vesicles at the early stages of endocytosis (12), through interaction with the WWY motif. DAB2 is down-regulated in majority of breast and ovarian cancers. Moreover, depletion and re-expression of DAB2 can trigger tumorigenesis or suppress growth, respectively (17). Therefore, DAB2 is considered as a tumor suppressor.

The selectivity of MVI for its binding partners is, in part, regulated by isoform splicing. The LI encodes an α -helix that sits upon, and therefore blocks, the RRL motif (18). This prevents partners, such as NDP52, interacting with the protein, and therefore the binding partner interactions of this isoform are driven by the WWY motif. In contrast, in the NI isoform, both the RRL and WWY motifs are available for binding. In this case, binding partner selectivity would be an important regula-

This work was supported by Medical Research Council Grant MR/M020606/1 and Science and Technology Facilities Council Grant 19130001. The authors declare that they have no conflicts of interest with the contents of this article.

This article contains Tables S1–S3 and Fig. S1–S3.

¹ These authors contributed equally to this work.

² To whom correspondence should be addressed: Sheffield Cancer Centre, Dept. of Oncology and Metabolism, University of Sheffield, Sheffield, S10 2RX, UK. E-mail: c.toseland@sheffield.ac.uk.

³ The abbreviations used are: MVI, myosin VI; CBD, cargo-binding domain; LI, large insert; SI, small insert; NI, non insert; ER, estrogen receptor; RFP, red fluorescent protein; qPCR, quantitative PCR.

This is an Open Access article under the CC BY license.

Binding partner regulation of myosin VI

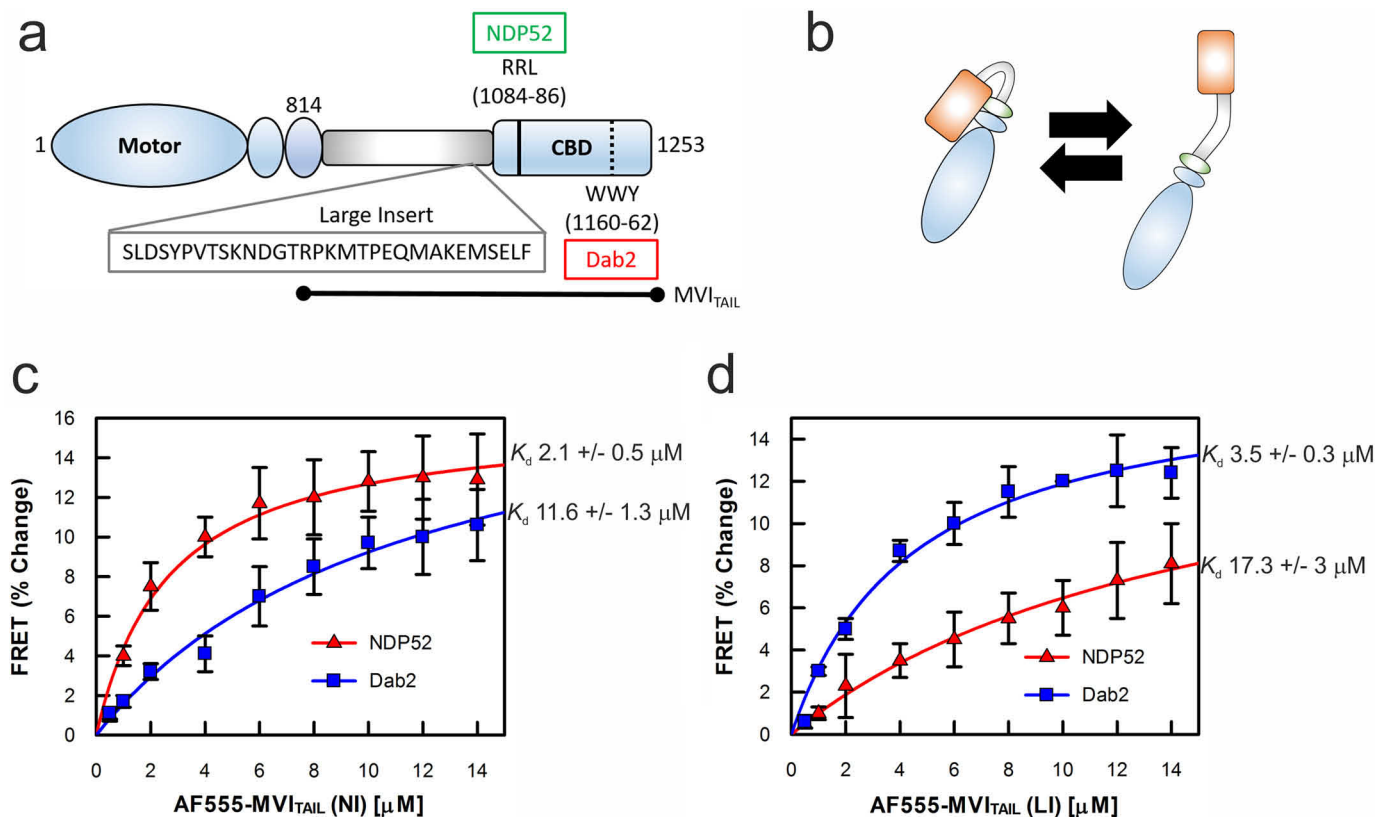


Figure 1. Interaction between myosin VI and binding partners NDP52 and DAB2. *a*, cartoon depiction of the key regions of the MVI_{TAIL}, as discussed in the text. This highlights the position of the large insert, along with the NDP52 and DAB2 binding sites. *b*, cartoon depiction of MVI backfolding with contacts between the CBD and motor, as described in Ref. 3. *c*, FRET titration of MVI_{TAIL(NI)} against 1 μM NDP52 (red triangles) or tDAB2 (blue squares). *d*, FRET titration of MVI_{TAIL(LI)} against 1 μM NDP52 (red triangles) or tDAB2 (blue squares). All titration data fitting was performed as described under "Materials and methods," giving a K_d as plotted. Error bars represent S.E. from three independent experiments.

tory mechanism. In the light of our recent work on the regulation of the NI isoform by NDP52 (3) and with the aim to unravel such a regulatory mechanism, we have established how competition between the two binding sites is achieved and how this can impact upon the role of nuclear MVI in gene expression.

Results

Interactions between binding partners and myosin VI

To establish how the selectivity of MVI for its binding partners is regulated, we compared its interactions with two binding partners, namely NDP52 and DAB2, as representatives of RRL- and WWY-binding proteins, respectively. Given our recent work on the interaction of the NI isoform with NDP52 (3); here we focus on the interaction with DAB2.

Before investigating the effect of DAB2 upon MVI, we first assessed their interaction. Recombinant full-length DAB2 was highly unstable and unable to yield sufficient amounts of protein for biochemical characterization. Therefore, we used the stable C-terminal region of the protein (residues 649–770), which contains the MVI binding site (12). This truncation of DAB2 will be referred to as tDAB2 throughout the manuscript, unless stated. To characterize the interaction between MVI and tDAB2, we performed an *in vitro* FRET assay by titrating Alexa 555–MVI_{TAIL(NI)} or Alexa 555–MVI_{TAIL(LI)} against FITC–DAB2. As demonstrated by the binding curves in Fig. 1 (*c* and

d), tDAB2 displayed relatively weak binding to the MVI_{TAIL(NI)} ($K_d = 11.6 \mu\text{M}$). Binding was noticeably enhanced for the MVI_{TAIL(LI)} ($K_d = 3.5 \mu\text{M}$), suggesting that the LI stabilizes the interaction with tDAB2. For comparison, measurements were also performed with NDP52. Consistent with the previous results (3), MVI_{TAIL(NI)} bound to NDP52 with a low micromolar affinity ($K_d = 2.1 \mu\text{M}$). In contrast, binding to the MVI_{TAIL(LI)} was over 8-fold weaker ($K_d = 17.3 \mu\text{M}$), indicating that NDP52 selectively interacts with MVI_{TAIL(NI)} rather than the MVI_{TAIL(LI)}. Based on these data, the differential affinity between the WWY and RRL sites suggests that the NI isoform would selectively bind RRL binding partners over its WWY competitors. In contrast, the LI isoform shows preferential binding to the WWY partners because the LI helix (i) masks the higher affinity RRL motif (18), thereby impeding NDP52 binding, and (ii) may provide additional interaction sites to increase the DAB2 affinity.

To further explore these interactions with full-length proteins, we assessed their association within cells. In HeLa cells, which only express the NI isoform (19), endogenous MVI shows little colocalization with endogenous DAB2, if any (Fig. 2*a*). In contrast, transiently expressed GFP-LI showed significant colocalization with endogenous DAB2, as highlighted by the 10-fold increase in Pearson's coefficient (Fig. 2, *b* and *d*). Consistent with the titration measurements, these observations

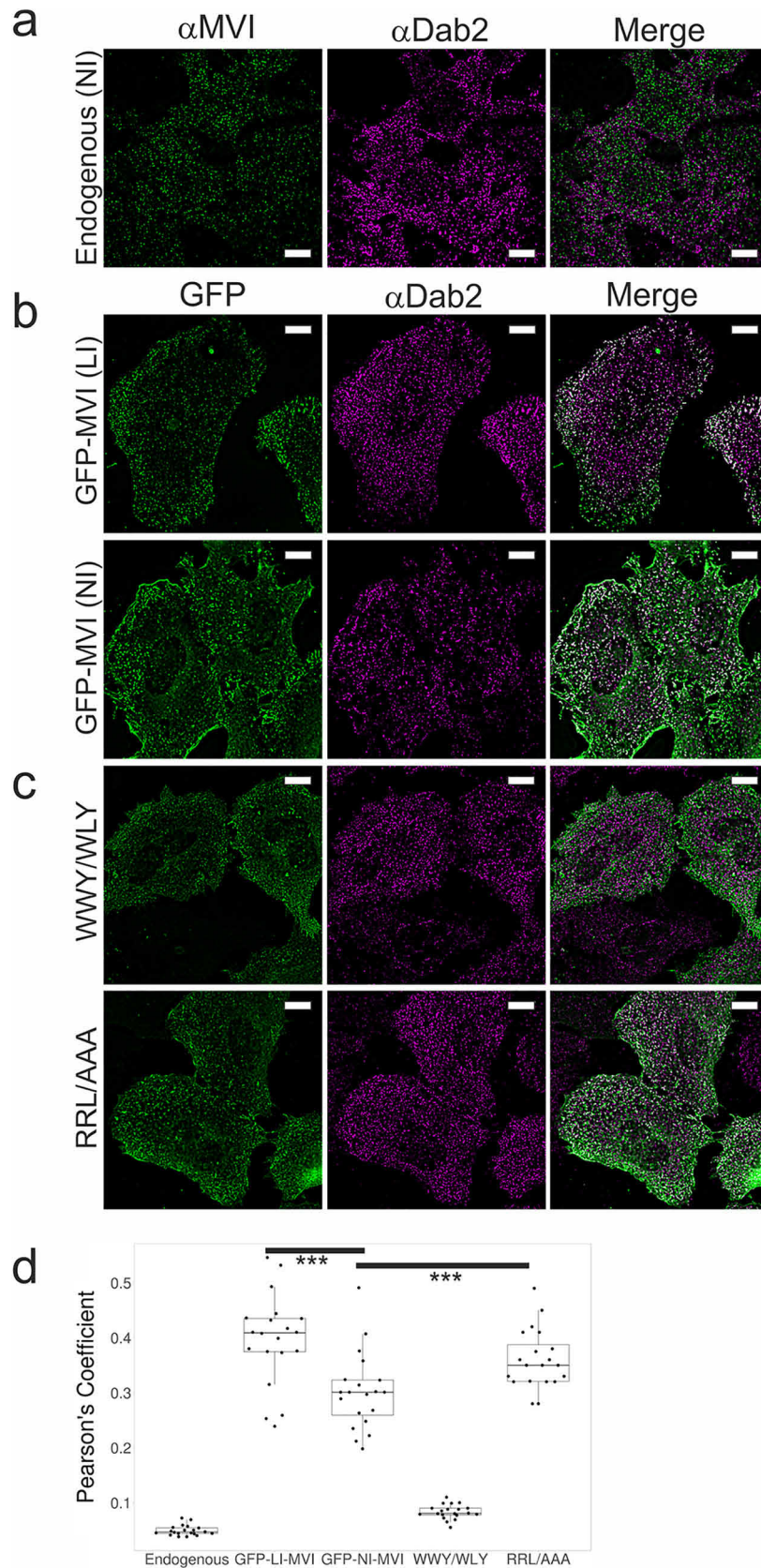


Figure 2. Myosin VI interaction with DAB2 in HeLa cells. *a*, immunofluorescence staining against MVI (green) and DAB2 (purple) in HeLa cells. White foci depict colocalization. *b*, representative images of transiently expressed NI- and LI-GFP-MVI in HeLa cells combined with immunofluorescence staining against DAB2. *c*, representative images of transiently expressed NI-MVI mutants WWY/WLY and RRL/AAA in HeLa cells combined with immunofluorescence staining against DAB2. Scale bars, 10 μ m in all images. *d*, Pearson's coefficient for MVI colocalization with DAB2 from images in *a*–*c*. The figure was generated using Ref. 26. Each data point represents a field of view consisting of 2–4 cells. *** represents a $p < 0.001$ by two-tailed t test.

Binding partner regulation of myosin VI

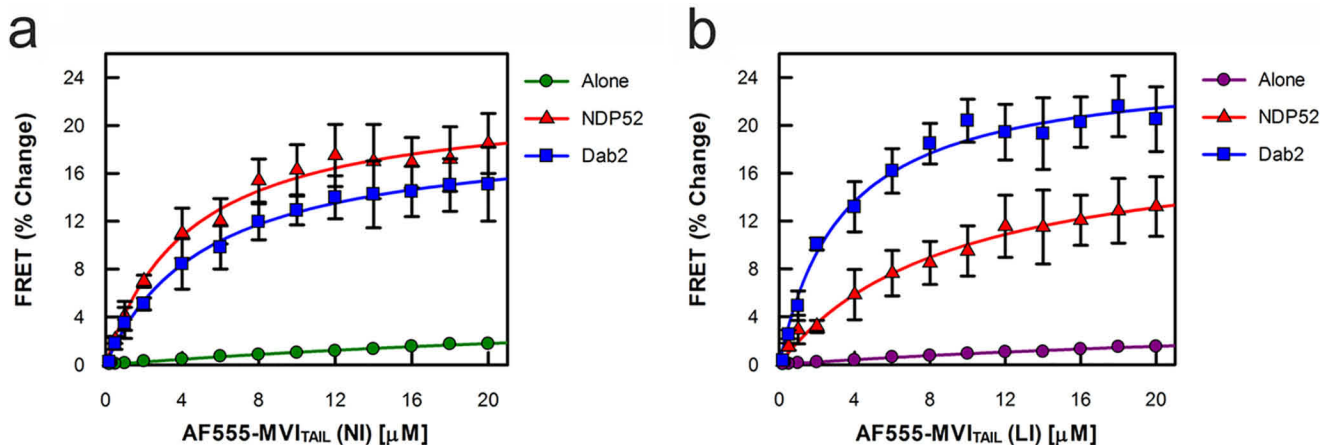


Figure 3. Binding partner–driven dimerization of myosin VI. *a*, FRET titration of AF555–MVI_{TAIL(NI)} against 1 μM FITC–MVI_{TAIL(NI)} \pm tDAB2 (20 μM) and NDP52 (20 μM). Data fitting generated NDP52 K_d^{DIMER} as 4.3 μM and tDAB2 K_d^{DIMER} as 5.3 μM . *b*, FRET titration of AF555–MVI_{TAIL(LI)} against 1 μM FITC–MVI_{TAIL(LI)} \pm tDAB2 (20 μM) and NDP52 (20 μM). Data fitting generated NDP52 K_d^{DIMER} as 9.3 μM and tDAB2 K_d^{DIMER} as 3.3 μM . All titration data fitting was performed as described under “Materials and methods.” (Error bars represent S.E. from three independent experiments.)

support that the selectivity of MVI for its partners differs depending on the isoform.

Our biochemical data suggested that the association of MVI with its partners is a concentration-dependent process. To address this in the cellular environment, we artificially increased the intracellular levels of the NI isoform by transient overexpression of GFP–NI–MVI and assessed its colocalization with endogenous DAB2. Consistent with our titration data, increase in the NI intracellular levels shifted the extent of colocalization between the two proteins at levels comparable with the LI–MVI (Fig. 2, *b* and *d*). To confirm the specificity of this observation, we also assessed the effect of transiently overexpressing two mutants of the NI isoform, each carrying mutations that abolish one of the two binding motifs (Fig. 2, *c* and *d*). As expected, GFP–NI–MVI (WWY/WLY), in which the WWY binding site is abolished, did not show any colocalization with DAB2. In contrast, mutation of the RRL motif did not affect the colocalization with DAB2. In fact, there was a slight increase in colocalization, which may relate to an increase in free MVI available to interact with WWY-binding partners. Overall, these observations are consistent with the conclusions from the titration measurements suggesting that significant interactions between the NI MVI_{TAIL} and tDAB2 can occur at higher protein concentrations. Therefore, our data support that the WWY-binding site has a weaker affinity for protein–protein interactions.

DAB2 mediates myosin VI large insert isoform dimerization

We have previously revealed how NDP52 interacts with MVI–NI to bring about its unfolding (3). Unfolding subsequently exposes dimerization sites, leading to protein oligomerization. However, the ability of the LI isoform to dimerize has not been yet explored. The presence of the additional α -helix in this isoform may perturb its dimerization. To test whether DAB2 can oligomerize both isoforms, we performed a FRET assay, whereby two pools of MVI_{TAIL(NI)} or MVI_{TAIL(LI)} were labeled, one with FITC and the other one with Alexa 555. Titrations revealed a weak association between the two tail pools (Fig. 3, *a* and *b*), consistent with our previous results

(3). Upon addition of 20 μM excess tDAB2, a change in FRET signal was observed, indicating the formation of a dimer complex. This occurred with both the NI and LI tails, with the LI signal being higher possibly because of the higher association with tDAB2. 20 μM excess of NDP52 was able to trigger dimerization of MVI_{TAIL(NI)} but failed to significantly dimerize the MVI_{TAIL(LI)}, consistent with the poor binding of NDP52 to the LI isoform.

Taking all our data together, we propose the following model: NDP52 specifically associates with MVI–NI through the RRL motif to trigger unfolding of the protein and subsequent dimerization. Similarly, binding of DAB2 to the LI isoform through the WWY motif also leads to dimerization. Although DAB2 has also the ability to bind the NI isoform, its weaker affinity for the WWY motif makes this interaction less favorable compared with the high-affinity binding of NDP52 to the RRL motif. In this way, the unfolding and dimerization of the NI isoform is preferentially assigned to the RRL binding partners.

Effect of binding partner competition upon the biochemical properties of nuclear myosin VI

We have shown that association of a binding partner with either the RRL or the WWY motif can bring about dimerization. We have also shown that the selectivity of MVI for its binding partners is regulated by the differential affinity between the two motifs. However, what is the biological impact of this binding partner selectivity and what would be the effect if it gets disrupted? More specifically, what is the effect of DAB2 upon the function of nuclear MVI, which we previously identified as the NI isoform? We have established that DAB2 can interact with this isoform at high protein concentrations. Interestingly, DAB2 can also be detected in the nucleus (Fig. 4*a*), and therefore it could interact with nuclear MVI.

We have previously shown that MVI contains a DNA-binding site on two conserved loops in the CBD (Fig. S1*a*) (3). These sites are only exposed upon unfolding of the tail domain, and therefore, DNA binding depends upon the interaction with a binding partner (3). First, we wanted to assess the effect of binding partners upon the ability of MVI to bind DNA, which is

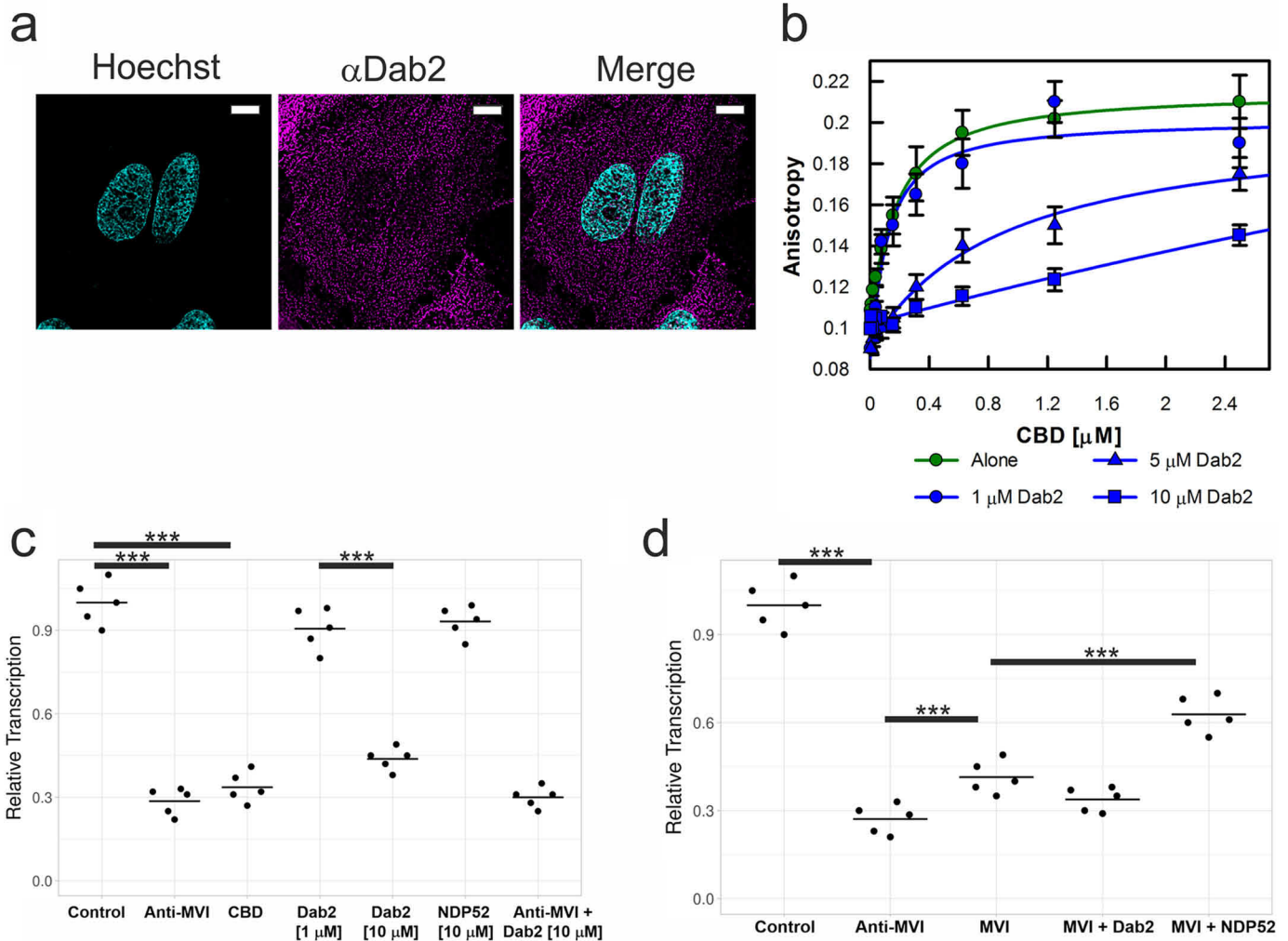


Figure 4. DAB2 represses the *in vitro* activity of nuclear myosin VI. *a*, immunofluorescence staining against DAB2 (purple) combined with DNA staining (cyan) in HeLa cells. Scale bar, 10 μm in all images. *b*, fluorescence anisotropy titrations of the CBD against a 40-bp fluorescein amidite–DNA (50 nM) with the highlighted concentrations of tDAB2. Data fitting was performed as described under “Materials and methods” ($K_d \pm \text{S.E.}$, $n = 3$ independent experiments). *c*, *in vitro* transcription by HeLaScribe extracts following antibody depletion as described under “Materials and methods” or in the presence of CBD at 25 μM , tDAB2 at 1 or 10 μM , and NDP52 at 10 μM . The samples were normalized to a nondepleted control reaction. *** represents a $p < 0.001$ by two-tailed *t* test. *d*, *in vitro* transcription following antibody depletion and rescue using recombinant MVI (NI) (1 μM), NDP52 (10 μM), or tDAB2 (10 μM), as described under “Materials and methods.” *** represents a $p < 0.001$ by two-tailed *t* test.

critical for its role in transcription (3). To determine DNA binding, we measured the fluorescence anisotropy of labeled DNA. As reported previously (3), NDP52 independently binds to DNA itself, and therefore, it is unsuitable for this purpose. In contrast, tDAB2 does not bind DNA (Fig. 1*b*), and therefore it can be used to determine its impact upon MVI binding DNA. To this end, we monitored the binding of MVI CBD to fluorescently labeled DNA (Fig. 4*b*). Whereas the CBD alone could bind to DNA with strong affinity ($K_d = 140$ nM), the presence of DAB2 inhibited DNA binding in a concentration-dependent manner. Interestingly, the DNA-binding sites of MVI are in close proximity to the WWY motif where DAB2 binds (Fig. S1*a*). Therefore, the interaction of DAB2 with MVI might induce a steric hindrance or a structural change within the CBD, which prevents the complex from binding DNA.

The ability of MVI to bind DNA is important for efficient *in vitro* transcription (3). Therefore, to assess the effect of DAB2 on the transcription activity of MVI, we performed *in vitro* transcription assays using the HeLaScribe nuclear extracts (Fig.

4*c*). Antibody depletion of MVI leads to a 70% decrease in transcription yield. A similar impact is achieved through the addition of recombinant CBD to displace MVI. Interestingly, addition of 10 μM recombinant tDAB2 leads to a 60% decrease in transcription. We therefore propose that this effect is due to tDAB2 interfering with the DNA-binding ability of MVI in the HeLaScribe lysate. This effect was observed in a concentration-dependent manner, consistent with our anisotropy data. The addition of 10 μM NDP52 did not decrease the transcription yield, suggesting that the tDAB2 effect is not due to sequestering MVI through binding to the protein. Moreover, no further decrease in transcription yield was found when tDAB2 was added following antibody depletion of MVI.

The compromised transcription activity that we observed following antibody depletion of MVI can be partially rescued through the addition of recombinant MVI (Fig. 4*d*). The addition of recombinant MVI and NDP52 together can restore transcription to $\sim 60\%$ (Fig. 4*d*), possibly because of the unfolding and dimerization of the protein. However, addition of recom-

Binding partner regulation of myosin VI

binant MVI and tDAB2 together failed to rescue the transcription yield, reinforcing that the observed effect is specific to DAB2, possibly through its interference with DNA binding. Taken together, our data suggest that DAB2 is a negative regulator of the transcription activity of MVI.

Effect of binding partner competition upon the nuclear functions of myosin VI

We have shown how two different binding partners can have contrasting effects on the biochemical properties and activity of MVI *in vitro*. On this basis, we then wanted to explore the impact of different binding partners on the cellular function of MVI and in particular its nuclear role in breast cancer cell line MCF-7. MVI is also distributed throughout the cell body, including the nucleus (Fig. 5a). In these cells, MVI has been already shown to be required for the expression of genes responsive to estrogen receptor (ER) signaling. When MCF-7 cells underwent siRNA knockdown of MVI or treatment with TIP, the small molecule inhibitor of MVI, there was a decrease in the expression of estrogen-activated *PS2* and *GREB1* (Fig. 5b). The impact of both treatments was similar, with a decrease of 70–80% for *PS2* and 30–40% for *GREB1*. Inhibition of MVI with TIP has already been shown to decrease the transcription yield *in vitro* (20). Based on our data, we can now suggest that the motor activity of MVI is required for ER signaling.

The genes that are under the control of the estrogen receptor relate, among others, to cell growth. Given the role of MVI in the expression of these genes, we then assessed the effect of MVI knockdown on MCF-7 growth (Fig. 5c). Indeed, the loss of MVI attenuates cell growth, which suggests there is a correlation between the role in gene expression and overall cell growth.

MCF-7 cells, along with many other estrogen receptor positive breast and ovarian cancer cell lines, have lost or attenuated DAB2 expression (Fig. S2a). Moreover, the reintroduction of DAB2 to these cell lines has been suggested to suppress tumorigenicity (17). Based upon the impact of MVI on the ER-driven gene expression and our *in vitro* data demonstrating the impact of DAB2 upon MVI associated transcription, we wished to explore whether reintroduction of DAB2 in MCF-7 could lead to a perturbation of in the expression of ER target genes. To this end, we transiently expressed full-length DAB2–mRFP in MCF-7 cells (Fig. S2, a and b) and then monitored the expression of *PS2* and *GREB1*. Interestingly, the presence of DAB2 in MCF-7 resulted in a 20–30% decrease in the expression of these ER-target genes.

To confirm that this decrease is due to the targeting of MVI, we transiently expressed in MCF-7 two truncations of DAB2 (Fig. S2c): the DAB2_{649–770} region, which contains the MVI binding site and is the one used in our biochemical assays, and the DAB2_{1–648}, which cannot associate with MVI (12). As expected, the DAB2_{649–770} resulted in a 40–50% decrease in the expression of the two ER target genes, whereas the DAB2_{1–648} did not have any effect, confirming that the observed decrease in gene expression is indeed due to the interaction of DAB2 with MVI. Overall, our observations suggest that DAB2 can function in the cell as a negative regulator of MVI in the expression of ER-target genes.

Discussion

The structural regulation of MVI controls its biochemical properties and therefore directly impacts on the cellular function of this motor protein. Here, we have explored what is the impact of binding partners on the conformation of MVI, how these interactions are regulated, and how this regulation varies between isoforms. We have then investigated how the selectivity of MVI for its binding partner can affect its biochemical properties and intracellular functions.

The structural regulation of MVI seems to follow a single general mechanism, which is summarized by the following model: MVI exists as a folded monomer that interacts with binding partners through the CBD. These interactions lead to MVI unfolding and subsequent dimerization of the protein through its tail domain. As shown previously, this generates a processive motor protein (3).

Moreover, here we have shown that this widely applied mechanism of structural regulation is under the control of a finely tuned interplay between binding partners and the MVI isoforms. In the case of the LI isoform, structural studies have revealed how the RRL motif is blocked by the LI helix (18), allowing only the WWY partners, such as DAB2, to bind to MVI. We have confirmed this here biochemically, by measuring the binding partner interactions at each site, using DAB2 as a representative example. In contrast, the NI isoform, in which both the RRL and WWY motif are readily accessible, should be able to associate with any partner. We have therefore explored the mechanism underlying the partner selectivity in this case. We have revealed that the NI isoform can enact selectivity through the differential affinity between the two sites, with the RRL motif having stronger binding affinity over the WWY. In this way, the selectivity for binding partners is based upon the relative concentration of WWY *versus* RRL partners, although the overall cellular concentrations of DAB2 is unlikely to be in the micromolar range. However, it is possible for there to be local high-protein concentrations, which can generate micromolar concentrations within a defined volume. In these instances interactions between MVI and binding partners would be observed. Moreover, cellular interactions may be supported by additional protein/cargo factors, thereby increasing the affinity. There could also be a global change in protein expression levels. For instance, the loss of a WWY partner would perturb the dynamics leading to an enhanced role of RRL binding partners.

This mechanism of selectivity is particularly relevant for the regulation of nuclear MVI, which is the NI isoform (3). Here, we have demonstrated the impact of a concentration-driven interaction with the low-affinity binding partner DAB2. Indeed, interaction with DAB2 blocked the ability of MVI to bind DNA and subsequently its transcription activity *in vitro*.

The impact of DAB2 of the biochemical properties of MVI raised questions about its impact on the cellular functions of MVI. DAB2 has been proposed to function as a tumor suppressor; however, the underlying mechanism remains elusive. Here, we have proposed that at least part of this activity could relate to the down-regulation of nuclear MVI in transcription. Because nuclear MVI is linked to estrogen receptor gene expression, this would in turn attenuate the activity of the estrogen receptor,

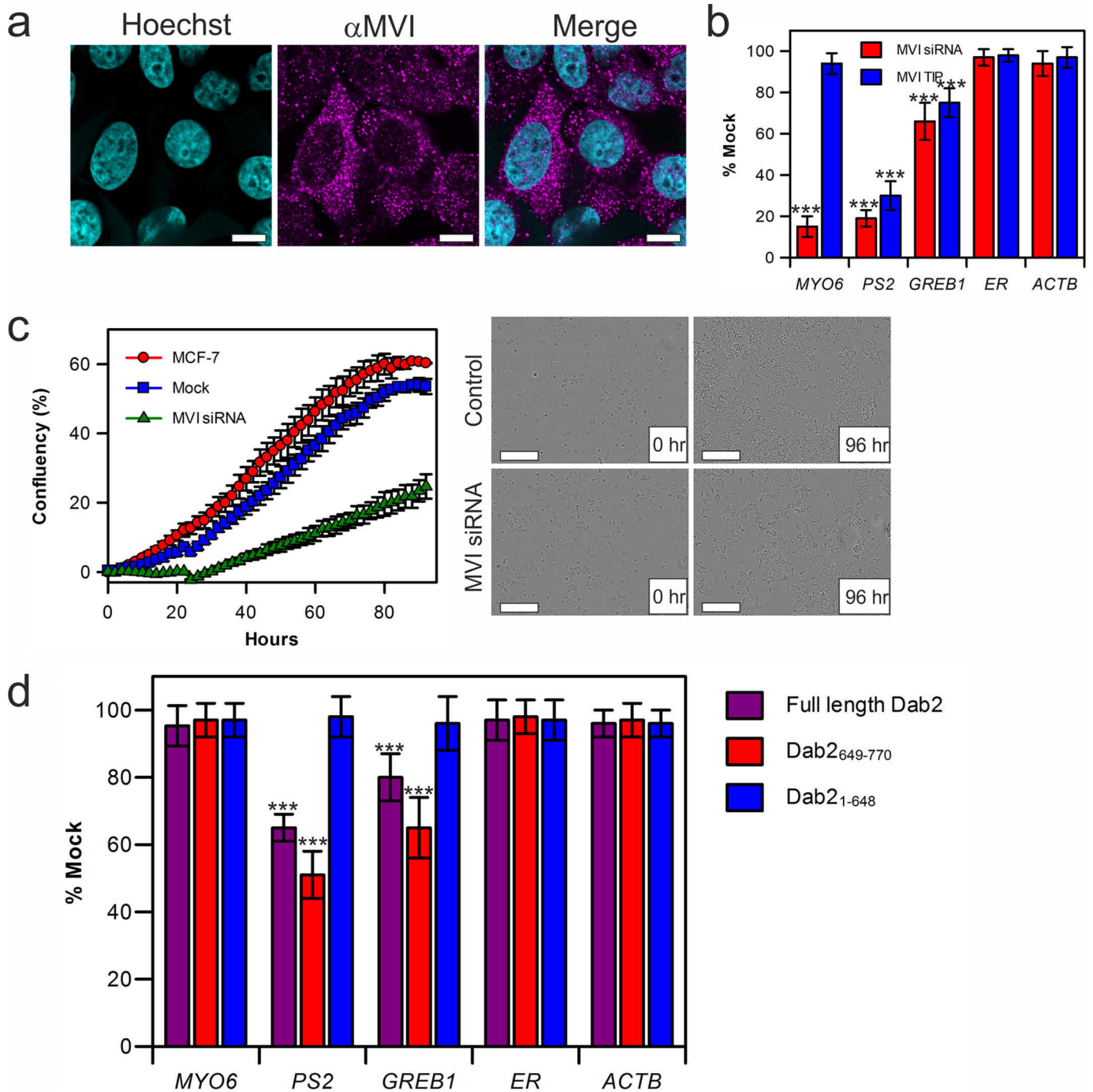


Figure 5. Inhibition of myosin VI in estrogen-linked gene expression. *a*, immunofluorescence staining against MVI (purple) combined with DNA staining (cyan) in MCF7 cells. Scale bar, 10 μ m in all images. *b*, expression of estrogen receptor gene targets following siRNA knockdown of MVI (red) or TIP treatment (blue) in MCF-7 cells. Expression is plotted as a percentage of expression in mock cells. *MYO6* reports on the success of the siRNA knockdown, whereas *ESR1* and *ACTB* were used to reflect global changes in transcription. *** represents a $p < 0.001$ by two-tailed *t* test. *c*, real-time growth of MCF-7 cells (red) and corresponding measurements following MVI siRNA knockdown (green) and mock transfection control (blue). The data represent three independent measurements, and error bars show S.E. Example images at start and end time points are shown. Scale bar, 300 μ m in all images. Western blot against DAB2 following transient transfection into MCF-7 cells is shown in Fig. S2a. *d*, Expression of estrogen receptor target genes following transient transfections of DAB2 (purple), DAB2₁₋₆₄₈ (blue), and DAB2₆₄₉₋₇₇₀ (red) in to MCF-7 cells. Expression is plotted as a percentage of expression in nontransfected cells. *MYO6*, *ESR1*, and *ACTB* were used to reflect global changes in transcription. (Error bars represent S.E. from three independent experiments. *** represents a $p < 0.001$ by two-tailed *t* test.)

subsequently leading to a decrease in tumorigenicity. Conversely, loss of a DAB2 would perturb the dynamics leading to an enhanced role of RRL binding partners, like NDP52 leading to enhanced MVI transcription activity. Cancer cell lines, such as the MCF-7, overexpress the NI isoform of MVI, which is the

one able to translocate to the nucleus, and they are therefore primed for transcriptional activity. This is further enhanced in MCF-7 cells by the loss of DAB2 expression, which relieves the DAB2-mediated negative regulation. Overall, this would lead to a high level of ER activity, which is MVI-dependent. Interest-

Binding partner regulation of myosin VI

ingly, reintroduction of DAB2 in these cells has an effect on their tumorigenic potential (17). In this study, we have confirmed that reintroduction of DAB2 perturbs the transcription landscape downstream the ER and revealed that this is due to MVI targeting. We therefore suggest that the down-regulation of the transcriptional activity of MVI is indeed part of the role of DAB2 as a tumor suppressor.

In summary, this study has allowed us to gain new insights into the regulation of MVI. The mechanism of selectivity of binding partners is isoform dependent. Although the LI-MVI employs a structural selection for its binding partners, the selectivity of the NI isoform is regulated by the relative expression levels of the partners. Finally, we provide an example of how the intracellular levels of MVI binding partners can modulate the cellular function of the protein. We propose that the tumor suppressor activity of DAB2 is, in part, related to the down-regulation of estrogen receptor target gene activation by nuclear MVI. These insights open new avenues for exploring how the activity of this multifunctional motor protein is regulated within the nucleus and the cytoplasm, as well.

Materials and methods

Constructs

Lists of constructs and PCR primers are provided in Tables S1 and S2, respectively. Constructs generated in this work are described below. The following human full-length myosin VI mutants (EGFP-C3-NI-MVI-RRL-AAA and EGFP-C3-NI-MVI-WWY-WLY) were a kind gift from F. Buss (Cambridge Institute for Medical Research). The full-length human DAB2-mRFP was isolated by PCR from pET28a-DAB2-RFP plasmid, restriction-digested with NheI and NotI, and cloned into the pZsGreen1-N1 backbone following removal of ZsGreen1. The human DAB2 truncations were generated by PCR isolation of the DAB2 fragment containing the myosin VI-binding site (aa 649–770) and the rest of DAB2 (aa 1–648), which does not contain the myosin VI-binding site from the above DAB2-mRFP plasmid. The PCRs were restriction-digested by XhoI and SacII and cloned into pEGFP-C3.

Protein expression and purification in *Escherichia coli*

Recombinant constructs were expressed in *E. coli* BL21 DE3 cells (Invitrogen) in Luria Bertani media. Proteins were purified by affinity chromatography (HisTrap FF; GE Healthcare). The purest fractions were further purified through a Superdex 200 16/600 column (GE Healthcare). Example gels are shown in Fig. S3.

Protein expression using *Baculovirus* system

Full-length myosin VI-NI and -LI and *Xenopus* calmodulin were expressed in Sf9 and Sf21 (*Spodoptera frugiperda*) insect cells using the Baculovirus expression system. Sf9 cells were cultured in suspension in sf900 medium (Gibco) at 27 °C to generate the P1–3 recombinant baculovirus stocks. Finally, expression of recombinant proteins was set up by infecting Sf21 cells with the P3 viral stock in ExCell 420 medium (Sigma). The cells were harvested by centrifugation (as above) for protein purification after 4 days. Prior to sonication, an additional 5 mg

of calmodulin was added with 2 mM DTT. After sonication, 5 mM ATP and 10 mM MgCl₂ were added, and the solution was rotated at 4 °C for 30 min before centrifugation (20,000 × g at 4 °C for 30 min). Then the cell lysate was subjected to the purification steps described above.

Protein labeling

Proteins were transferred into 50 mM sodium phosphate (pH 6.5) using a PD10 desalting column. The samples were then incubated with a 5-fold excess of dye for 4 h, rotating at 4 °C. Excess dye was removed using a PD10 desalting column pre-equilibrated with 50 mM sodium phosphate, 150 mM NaCl, and 1 mM DTT. Labeling efficiency was calculated based on the absorbance at 280 nm and the absorbance maximum of the dye. Typical efficiency was 90%, whereby the less than complete labeling was taken as an indicator for a single dye per protein. This was tested for isolated preparations in MS, which revealed both an unlabeled and single labeled population.

Cell culture and transfection

HeLa (ECACC 93021013) and MCF7 (ECACC 86012803) cells were cultured at 37 °C and 5% CO₂, in Gibco α -minimum Eagle's medium with GlutaMAX (no nucleosides), supplemented with 10% fetal bovine serum (Gibco), 100 units/ml penicillin, and 100 μ g/ml streptomycin (Gibco). For the transient expression of MVI isoforms and mutants, full-length DAB2, and truncations, HeLa cells and/or MCF7 cells grown on glass coverslips were transfected with EGFP-NI-MVI, EGFP-LI-MVI, EGFP-NI-MVI-RRL-AAA, EGFP-NI-MVI-WWY-WLY, DAB2-mRFP, EGFP-DAB2-1-648, and EGFP-DAB2-649-770 constructs using Lipofectamine 2000 (Invitrogen), following the manufacturer's instructions. Depending on the construct, 24–72 h after transfection, the cells were subjected to nuclear staining using Hoechst 33342 (Thermo Scientific), fixed, and analyzed or subjected to indirect immunofluorescence (see below).

Full-length DAB2-RFP cDNA was electroporated into MCF7 cells using Bio-Rad Gene Pulser Xcell™ electroporation system. After trypsinization, harvested cells were washed with 1 × PBS and counted; 1.5 × 10⁶ cells were resuspended in 800 μ l of cold Opti-MEM medium; and the cell suspension was kept on ice. 10 μ g of DNA was added to the cell suspension, and the mixture was transferred to the Bio-Rad 4-mm cuvette. The cells were then pulsed using exponential-decay protocol with a voltage of 300 V and a capacitance of 350 microfarads. The cells were allowed to recover for 5 min, after which warm complete medium (minimum Eagle's medium) was added to them, and they were plated in a 6-well plate at a density of 0.5 × 10⁶ cells/well. The cells were collected for protein or RNA extraction after 48 h.

Immunofluorescence

Transfected and nontransfected HeLa or MCF-7 cells were fixed for 15 min at room temperature in 4% (w/v) paraformaldehyde, and residual paraformaldehyde was quenched for 15 min with 50 mM ammonium chloride. All subsequent steps were performed at room temperature. The cells were permeabilized and simultaneously blocked for 15 min with 0.1% (v/v)

Triton X-100 and 2% (w/v) BSA in PBS. The cells were then immunostained against the endogenous proteins by 1 h of incubation with the indicated primary and subsequently the appropriate fluorophore-conjugated secondary antibody (details below), both diluted in 2% (w/v) BSA in PBS. The following antibodies were used at the indicated dilutions: rabbit anti-MVI (1:200, Atlas–Sigma HPA0354863–100UL), mouse anti-DAB2 (1:100, Abcam ab88590), donkey anti-mouse Alexa Fluor 488–conjugated (1:500, Abcam Ab181289), donkey anti-mouse Alexa Fluor 555–conjugated (1:500, Abcam Ab150110), donkey anti-rabbit Alexa Fluor 488–conjugated antibody (1:500, Abcam Ab181346), and donkey anti-rabbit Alexa Fluor 555–conjugated antibody (1:500, Abcam Ab150074). Coverslips were mounted on microscope slides with Mowiol (10% (w/v) Mowiol 4–88, 25% (w/v) glycerol, 0.2 M Tris-HCl, pH 8.5), supplemented with 2.5% (w/v) of the anti-fading reagent DABCO (Sigma).

For colocalization analysis, 20 fields of view were recorded with 2–4 cells/field. We ensured that all cells were transfected within the field. Pearson's coefficients were obtained with the JACoP plugin (21) for ImageJ.

Immunoblot analysis

The total protein concentration was determined by Bradford assay (Sigma) following the manufacturer's instructions. Cell lysates were heat-denatured and resolved by SDS-PAGE. The membrane was probed against the endogenous proteins by incubation with mouse anti-DAB2 polyclonal antibody (1:1000, Abcam ab88590) and subsequently a goat anti-mouse antibody coupled to horseradish peroxidase (1:15,000, Abcam ab97023). The bands were visualized using the ECL Western blotting detection reagents (Invitrogen), and the images were taken using Syngene GBox system. Images were processed in ImageJ.

Fluorescence imaging

The cells were visualized using either the Zeiss LSM 880 confocal microscope or the wide-field Olympus IX71 microscope. The former was equipped with a Plan-Apochromat 63× 1.4 NA oil immersion lens (Carl Zeiss, 420782-9900-000). Three laser lines, *i.e.* 405, 488, and 561 nm, were used to excite the fluorophores, *i.e.* Hoechst, GFP, and RFP, respectively. The built-in dichroic mirrors (Carl Zeiss, MBS-405, MBS-488, and MBS-561) were used to reflect the excitation laser beams on to cell samples. The emission spectral bands for fluorescence collection were 410–524 nm (Hoechst), 493–578 nm (GFP) and 564–697 nm (RFP). The detectors consisted of two multianode photomultiplier tubes and one gallium arsenide phosphide detector. The green channel (GFP) was imaged using the gallium arsenide phosphide detector, whereas the blue (Hoechst) and red (RFP) channels were imaged using multianode photomultiplier tubes. ZEN software (Carl Zeiss, ZEN 2.3) was used to acquire and render the confocal images. The later was equipped with an PlanApo 100× OTIRFM-SP 1.49 NA lens mounted on a PIFOC *z* axis focus drive (Physik Instrumente, Karlsruhe, Germany), and illuminated with an automated 300W Xenon light source (Sutter, Novato, CA) with appropriate filters (Chroma, Bellows Falls, VT). The images were acquired using a QuantEM (Photometrics) EMCCD camera,

controlled by the Metamorph software (Molecular Devices). The whole volume of cells was imaged by acquiring images at *z*-steps of 200 nm. Wide-field images were deconvolved with the Huygens Essential version 17.10 software. Confocal images were deconvolved using the Zeiss Zen2.3 Blue software, using the regularized inverse filter method. All images were then analyzed by ImageJ.

IncuCyte

The cells were seeded onto 96-well tissue culture dishes at equal densities in six replicates. After attachment overnight, the cells were transfected with MVI siRNA. Photomicrographs were taken every hour using an IncuCyte live cell imager (Essen Biosciences, Ann Harbor, MI), and confluency of cultures was measured using IncuCyte software. Confluency values between wells were normalized to initial confluency for comparison.

RNA extraction and RT-qPCR

RNA from DAB2-RFP transfected or nontransfected MCF7 cells was extracted using Gene Jet RNA purification kit (Thermo scientific) according to the manufacturer's protocol. The RNA concentration was measured using a Geneflow nanophotometer and RT-qPCR was performed with one-step QuantiFast SYBR Green qPCR kit (Qiagen) using 50 ng of RNA in each sample. A list of qPCR primers is given in Table S3.

DNA substrates

DNA substrate ds40 consisted of labeled (TTAGTTGTTCTGTAGTGCTCGTCTGGCTCTGGATTACCCGC*FAM) and unlabeled (GCGGGTAATCCAGAGCCAGACGAGCACTACGAACAATA) oligonucleotides purchased from IDT. To form duplex DNA substrates, the oligonucleotides were mixed at equimolar concentrations at either 50 μ M in water or a buffer containing 50 mM Tris·HCl (pH 7.5), 150 mM NaCl, and 3 mM MgCl₂.

In vitro transcription

The DNA template was the pEGFP-C3 linearized plasmid containing the cytomegalovirus promoter, which would generate a 130-base run-off transcript. The HeLaScribe (Promega) reactions were performed in triplicate, through two independent experiments, according to the manufacturer's instructions. The reactions were performed for 60 min at 25 °C.

The reactions were also performed following preclearance with the MVI antibody. Protein G Dynabeads (Invitrogen) were prepared according to the manufacturer's instructions before being loaded with 4 μ g of antibody. The samples were incubated for 30 min on ice, and beads were extracted immediately before performing the transcription reaction. For quantification, mRNA was purified using a Gene Jet RNA purification kit (Thermo scientific) according to the manufacturer's protocol, and RT-qPCR was performed with a one-step QuantiFast SYBR Green qPCR kit (Qiagen).

Titration measurements

All reactions were performed at 25 °C in a buffer containing 50 mM Tris·HCl (pH 7.5), 150 mM sodium chloride, and 1

Binding partner regulation of myosin VI

mM DTT in a final volume of 100 μ l. Measurements were performed using a ClarioStar plate reader (BMG Labtech).

Intensity measurements were performed at the following wavelengths: FITC (excitation, 490 nm) and Alexa Fluor 555 (excitation, 555 nm). FITC to Alexa Fluor 555 FRET measurements were performed using the wavelength excitation of 470 nm and the emission of 575 nm. Anisotropy was measured with the instrument in the T format, allowing simultaneous acquisition of parallel (I_{\parallel}) and perpendicular (I) components using BMG filter sets for fluorescein (excitation, 482/16-10, Dichroic LP504; and emission, 530/-40).

Analysis of kinetic data

For fluorescence anisotropy titrations: Anisotropy was calculated, as described below, based upon established procedures (22–25).

Total fluorescence intensity (F_t) is given by the following.

$$F_t = \sum c_i F_i \quad (\text{Eq. 1})$$

Total anisotropy (A_t) is given by the following,

$$A_t = \frac{\sum c_i F_i A_i}{F_t} \quad (\text{Eq. 2})$$

where c_i is the concentration of species i , F_i is the fluorescence intensity per unit of concentration, and A_i is the anisotropy. This is calculated from the parallel and perpendicular fluorescence intensity (I) in relation to the plane of excitation by the following.

$$A_i = \frac{I_{\parallel} - I_{\perp}}{I_{\parallel} + 2I_{\perp}} \quad (\text{Eq. 3})$$

Because anisotropy is additive for multiple fluorescence species in solution, it is used to give a measure of their relative concentrations. For MVI (and various constructs) there are two fluorescence species: DNA and MVI·DNA. The total anisotropy can then be calculated in terms of the dissociation constant (K_d) for the MVI·DNA complex,

$$A_t = \frac{A_{\text{DNA}}([\text{DNA}]_t - [\text{MVI}\cdot\text{DNA}]) + A_{\text{MVI}\cdot\text{DNA}} Q [\text{MVI}\cdot\text{DNA}]}{[\text{DNA}]_t - [\text{MVI}\cdot\text{DNA}] + Q [\text{MVI}\cdot\text{DNA}]} \quad (\text{Eq. 4})$$

where

$$[\text{MVI}\cdot\text{DNA}] = \frac{([\text{MVI}]_t + [\text{DNA}]_t + K_d) - \sqrt{([\text{MVI}]_t + [\text{DNA}]_t + K_d)^2 - 4[\text{MVI}]_t[\text{DNA}]_t}}{2} \quad (\text{Eq. 5})$$

and where $[\text{MVI}]_t$ and $[\text{DNA}]_t$ are the total concentrations for each reactant. $[\text{MVI}\cdot\text{DNA}]$ is the concentration of the protein-bound DNA complex. Q is the fluorescence intensity of MVI·DNA relative to DNA. The anisotropy data were fitted to obtain dissociation constants based on the above equations using GraFit fitting software (27).

For the FRET titrations, the 575-nm intensity data were corrected for the increase in intensity caused by a small direct excitation. This background signal was subtracted from the dataset to leave the FRET values. The titration curves for the MVI_{TAIL} interactions were fitting to a binding quadratic equation.

[Complex]

$$= \frac{([\text{FITC}]_t + [\text{AF555}]_t + K_d) - \sqrt{([\text{FITC}]_t + [\text{AF555}]_t + K_d)^2 - 4[\text{FITC}]_t[\text{AF555}]_t}}{2} \quad (\text{Eq. 6})$$

Data availability

The data supporting the findings of this study are available from the corresponding author on request.

Author contributions—N. F., Y. H.-G., B. Aston, and C. P. T. conceptualization; N. F., Y. H.-G., B. Aston, Á. d. S., R. E. G., and C. P. T. formal analysis; N. F., Y. H.-G., and C. P. T. supervision; N. F., Y. H.-G., and C. P. T. funding acquisition; N. F., Y. H.-G., B. Aston, Á. d. S., R. E. G., B. Alamad, L. W., and C. P. T. investigation; N. F., Y. H.-G., and C. P. T. writing-original draft; N. F., Y. H.-G., B. Aston, and C. P. T. writing-review and editing; L. W., M. L. M.-F., and C. P. T. resources.

Acknowledgments—We thank Darren Griffin and Anastasios Tsaousis for sharing of equipment.

References

- Roberts, R., Lister, I., Schmitz, S., Walker, M., Veigel, C., Trinick, J., Buss, F., and Kendrick-Jones, J. (2004) Myosin VI: cellular functions and motor properties. *Philos. Trans. R. Soc. Lond. B Biol. Sci.* **359**, 1931–1944 [CrossRef Medline](#)
- Vreugde, S., Ferrai, C., Miluzio, A., Hauben, E., Marchisio, P. C., Crippa, M. P., Bussi, M., and Biffo, S. (2006) Nuclear myosin VI enhances RNA polymerase II-dependent transcription. *Mol. Cell* **23**, 749–755 [CrossRef Medline](#)
- Fili, N., Hari-Gupta, Y., Dos Santos, Á., Cook, A., Poland, S., Ameer-Beg, S. M., Parsons, M., and Toseland, C. P. (2017) NDP52 activates nuclear myosin VI to enhance RNA polymerase II transcription. *Nat. Commun.* **8**, 1871 [CrossRef Medline](#)
- Avraham, K. B., Hasson, T., Steel, K. P., Kingsley, D. M., Russell, L. B., Mooseker, M. S., Copeland, N. G., and Jenkins, N. A. (1995) The mouse Snell's waltzer deafness gene encodes an unconventional myosin required for structural integrity of inner ear hair cells. *Nat. Genet.* **11**, 369–375 [CrossRef Medline](#)
- Dunn, T. A., Chen, S., Faith, D. A., Hicks, J. L., Platz, E. A., Chen, Y., Ewing, C. M., Sauvageot, J., Isaacs, W. B., De Marzo, A. M., and Luo, J. (2006) A novel role of myosin VI in human prostate cancer. *Am. J. Pathol.* **169**, 1843–1854 [CrossRef Medline](#)
- Mohiddin, S. A., Ahmed, Z. M., Griffith, A. J., Tripodi, D., Friedman, T. B., Fananapazir, L., and Morell, R. J. (2004) Novel association of hypertrophic cardiomyopathy, sensorineural deafness, and a mutation in unconventional myosin VI (MYO6). *J. Med. Genet.* **41**, 309–314 [CrossRef Medline](#)
- Yoshida, H., Cheng, W., Hung, J., Montell, D., Geisbrecht, E., Rosen, D., Liu, J., and Naora, H. (2004) Lessons from border cell migration in the *Drosophila* ovary: a role for myosin VI in dissemination of human ovarian cancer. *Proc. Natl. Acad. Sci. U.S.A.* **101**, 8144–8149 [CrossRef Medline](#)
- Buss, F., Arden, S. D., Lindsay, M., Luzio, J. P., and Kendrick-Jones, J. (2001) Myosin VI isoform localized to clathrin-coated vesicles with a role in clathrin-mediated endocytosis. *EMBO J.* **20**, 3676–3684 [CrossRef Medline](#)
- Au, J. S., Puri, C., Ihrke, G., Kendrick-Jones, J., and Buss, F. (2007) Myosin VI is required for sorting of AP-1B-dependent cargo to the basolateral

- domain in polarized MDCK cells. *J. Cell Biol.* **177**, 103–114 [CrossRef](#) [Medline](#)
10. Morriswood, B., Ryzhakov, G., Puri, C., Arden, S. D., Roberts, R., Dendrou, C., Kendrick-Jones, J., and Buss, F. (2007) T6BP and NDP52 are myosin VI binding partners with potential roles in cytokine signalling and cell adhesion. *J. Cell Sci.* **120**, 2574–2585 [CrossRef](#) [Medline](#)
 11. Naccache, S. N., Hasson, T., and Horowitz, A. (2006) Binding of internalized receptors to the PDZ domain of GIPC/synectin recruits myosin VI to endocytic vesicles. *Proc. Natl. Acad. Sci. U.S.A.* **103**, 12735–12740 [CrossRef](#) [Medline](#)
 12. Spudich, G., Chibalina, M. V., Au, J. S., Arden, S. D., Buss, F., and Kendrick-Jones, J. (2007) Myosin VI targeting to clathrin-coated structures and dimerization is mediated by binding to Disabled-2 and PtdIns(4,5)P₂. *Nat. Cell Biol.* **9**, 176–183 [CrossRef](#) [Medline](#)
 13. Koriath, F., Gieffers, C., Maul, G. G., and Frey, J. (1995) Molecular characterization of NDP52, a novel protein of the nuclear domain 10, which is redistributed upon virus infection and interferon treatment. *J. Cell Biol.* **130**, 1–13 [CrossRef](#) [Medline](#)
 14. Sternsdorf, T., Jensen, K., Züchner, D., and Will, H. (1997) Cellular localization, expression, and structure of the nuclear dot protein 52. *J. Cell Biol.* **138**, 435–448 [CrossRef](#) [Medline](#)
 15. Mostowy, S., Sancho-Shimizu, V., Hamon, M. A., Simeone, R., Brosch, R., Johansen, T., and Cossart, P. (2011) p62 and NDP52 proteins target intracytosolic Shigella and Listeria to different autophagy pathways. *J. Biol. Chem.* **286**, 26987–26995 [CrossRef](#) [Medline](#)
 16. Yang, C. K., Kim, J. H., and Stallcup, M. R. (2006) Role of the N-terminal activation domain of the coiled-coil coactivator in mediating transcriptional activation by β -catenin. *Mol. Endocrinol.* **20**, 3251–3262 [CrossRef](#) [Medline](#)
 17. He, J., Smith, E. R., and Xu, X. X. (2001) Disabled-2 exerts its tumor suppressor activity by uncoupling c-Fos expression and MAP kinase activation. *J. Biol. Chem.* **276**, 26814–26818 [CrossRef](#) [Medline](#)
 18. Wollscheid, H. P., Biancospino, M., He, F., Magistrati, E., Molteni, E., Lupia, M., Soffientini, P., Rottner, K., Cavallaro, U., Pozzoli, U., Mapelli, M., Walters, K. J., and Polo, S. (2016) Diverse functions of myosin VI elucidated by an isoform-specific α -helix domain. *Nat. Struct. Mol. Biol.* **23**, 300–308 [CrossRef](#) [Medline](#)
 19. Puri, C., Chibalina, M. V., Arden, S. D., Kruppa, A. J., Kendrick-Jones, J., and Buss, F. (2010) Overexpression of myosin VI in prostate cancer cells enhances PSA and VEGF secretion, but has no effect on endocytosis. *Oncogene* **29**, 188–200 [CrossRef](#) [Medline](#)
 20. Cook, A., Hari-Gupta, Y., and Toseland, C. P. (2018) Application of the SSB biosensor to study in vitro transcription. *Biochem. Biophys. Res. Commun.* **496**, 820–825 [CrossRef](#) [Medline](#)
 21. Bolte, S., and Cordelieres, F. P. (2006) A guided tour into subcellular colocalization analysis in light microscopy. *J. Microsc.* **224**, 213–232 [CrossRef](#) [Medline](#)
 22. Brownbridge, G. G., Lowe, P. N., Moore, K. J., Skinner, R. H., and Webb, M. R. (1993) Interaction of GTPase activating proteins (GAPs) with p21ras measured by a novel fluorescence anisotropy method. Essential role of Arg-903 of GAP in activation of GTP hydrolysis on p21ras. *J. Biol. Chem.* **268**, 10914–10919 [Medline](#)
 23. Soh, Y. M., Bürmann, F., Shin, H. C., Oda, T., Jin, K. S., Toseland, C. P., Kim, C., Lee, H., Kim, S. J., Kong, M. S., Durand-Diebold, M. L., Kim, Y. G., Kim, H. M., Lee, N. K., Sato, M., *et al.* (2015) Molecular basis for SMC rod formation and its dissolution upon DNA binding. *Mol. Cell* **57**, 290–303 [CrossRef](#) [Medline](#)
 24. Toseland, C. P. (2014) Fluorescence to study the ATPase mechanism of motor proteins. *Exs* **105**, 67–86 [Medline](#)
 25. Toseland, C. P., and Geeves, M. A. (2014) Rapid reaction kinetic techniques. *Exs* **105**, 49–65 [Medline](#)
 26. Postma, M., and Goedhart, J. (2019) PlotsOfData: a web app for visualizing data together with their summaries. *PLoS Biol.* **17**, e3000202 [CrossRef](#) [Medline](#)
 27. Leatherbarrow, R. J. (2001) *Grafit*, version 5, Erithacus Software Ltd., Hove, UK